Electrochemical Detection of Dissolved Ce in Water Using Boron-Doped Diamond Electrode

H Akrout[1*], S Maximovitch[2]

[1]*Department of Laboratory of Wastewater Treatment, Centre of Water Research and Technologies (CERTE), Echopark Borj Cedria, Soliman, Tunisia;* [2]*Department of Laboratory of Electrochemistry and Physico-chemistry of Materials and Interfaces, INPG-CNRS, Saint-Martin-d'Hères Cedex, France*

ABSTRACT

A comparative study of the electrochemical behavior and structural characteristics of boron-doped diamond electrode before and after working under high anodic potential conditions in aqueous acidic solution is performed. No changes can be detected on Mott-Schottky plots nor on micro-Raman images after a 500 hours working. The high stability of such a surface as probed by the structure-reactivity relationship is also revealed with the unmodified electrochemical response to the Ce^{3+}/Ce^{4+} redox couple.

Keywords: Boron-doped diamond; Cerium; Ageing; Electrochemical

INTRODUCTION

Boron-doped diamond is an attractive electrode material due to its high stability in strong acidic or alkaline media, low background current, wide potential window and high over-potential for oxygen evolution during anodic oxidation in aqueous solutions [1]. It could be used in dosage of element with high electrochemical potential in conditions of extremely acidity or basicity [2]. They promote also the electro-oxidation of organics and high contents of inorganic for wastewater treatment [2-6].

Recently, several reports have presented the electrochemical response of boron-doped diamond electrodes to the ceric/cerous redox couple in aqueous acidic solutions [7,8] on BDD. The Ce^{3+}/Ce^{4+} redox couple has a more positive standard potential than that of the H_2O/H_2 couple and due to this very positive potential, the electrochemical investigations are scarce, the signal related to the oxidation of the Ce^{3+} being not visible or in the best case, superimposed on the water oxidation current. The studies performed were carried out to investigate the kinetic parameters for the anodic oxidation of Ce^{3+} mainly by use of cyclic voltammetry, or the electron transfer rate at BDD in comparison to the one at gold surfaces [9].

In the present work, we have investigated the boron-doped diamond electrode behavior in HNO_3 solutions with the time working in order to detect any eventual modification of the electrochemical characteristics and damage of the surface generated under high anodic potential and long working conditions. The electrochemical responses of the Ce^{3+}/Ce^{4+} couple at the BDD electrode were analyzed by cyclic voltammetry measurements and its semiconductor characteristics by Mott-Schottky plots.

In order to relate variations of the electrochemical response of the BDD electrode recorded with the working time to eventual damages or modifications of the surface generated during the anodic oxidation, the surface of the electrode was analysed by Scanning Electron Microscopy. The crystal structure and dopant concentration were analysed by Raman imagery and micro-Raman spectroscopy and the chemical nature of the surface by X-ray photoelectron spectroscopy measurements before and after different working steps

MATERIALS AND METHODS

Diamond synthesis

Polycrystalline diamond layers were synthesised on silicon high purity p-type wafer by microwave plasma enhanced chemical vapour deposition in a conventional reactor [10]. The growth conditions used were as follows: substrate temperature: 700℃ -900℃; total gas flow of a mixture of 0.7% methane in hydrogen: 100 sccm; total pressure in the reactor: 20 torr (30 mbar), microwave power: 700 W. The dopant source was boron oxide set in a Pt crucible put on the substrate holder near the silicon substrate. Prior to the diamond growth, the silicon substrate were ultrasonically damaged with diamond powder in ethanol in order to improve the nucleation density [11]. After deposition, the methane flow was stopped and the films remained exposed to the hydrogen plasma for an additional time of 30 min. The film thickness, after 72 hours of

deposition averaged 25 μm. Dopant concentration in the diamond layers, as estimated from Raman spectroscopy measurements was in the range of 10^{18} cm^{-3} to 10^{20} cm^{-3} [12]. The film resistivity was equal to or less than 1 Ω cm as measured with a four-point probe. The polycrystalline diamond film consists of randomly oriented crystallites of few microns size and with predominantly cubic (100) and triangular (111) faces. No other trace of any elements than carbon or oxygen was found by XPS on the diamond surface.

Electrochemical set up

BDD was deposited on Silicium 'bastille' of 10 mm diameter. The contact surface is limited to 0.28 cm². Voltamperometry measurements were performed using Potentiostat/galvanostat (EG & G Model 273 A), standard electrochemical cell of 200 mL was used with three electrode arrangement. Counter electrode was Platinum and reference electrode was Saturated Calomel (SCE). Electrochemistry Impedance Spectroscopy (SIE) was performed potentiostat Solartron 1286 and transfer fonction analyzer Solartron 1260 (Z plot software).

BDD electrode ageing was undertaken HNO$_3$ 2 M solution at anodic current density 100 mA cm-2. Different ageing steps were fixed (0, 50, 218, 340, 530 hours). Electrode reactivity was examined by anodic peak obtained with cerium (Ce^{3+}/Ce^{4+}) in HNO$_3$ 2 M+Ce(NO$_3$)$_3$ 0.1 M on voltamperometry and with Mott-Schottky diagram.

Mott-Schottky diagrams were performed in HNO$_3$ 2 M solutions using SIE measured at decreasing potential from 2.3 V à 0.5 V at each 100 mV. Electrode activation is assured by anodic treatment at 30 mA before each measurement for 60 s.

Many electrodes are prepared at same conditions. Cerium Oxidation peak is measured with new electrode and even electrode with ageing action (a). Mott-Schottky diagrams are plotted with electrode at different step of ageing. Mott-Scottky diagrams, at initial state, are performed with other electrode (c). At this condition, Impedance measurements are carried out at increasing potential in order to detect the behavior before oxidation.

New BDD electrodes are cleaned beforehand with short anodic oxidation (30 s).

Raman spectroscopy measurements

Raman microprobe spectra were recorded on a Jobin-Yvon/Horiba T64000 triple monochromator with a N$_2$ cooled CCD detector and a microscope equipped with a computer-driven XY table which allows getting images: All spectra recorded for each of the different probed points were collected to compose high resolution (x100 objective, 1 μm step) 2D cartographies. Thanks to the confocal optics, the higher magnification allowed depth of probed field to be reduce to about 2-4 μm for a 0.7 μm spot size. The 514.5 nm line of an ArKr$^+$ laser was used as excitation source. The stability of the spectrometer over the acquisition time (5 to 8 hours) for complete image guaranteed wave number shift accuracy better than 0.2 cm^{-1}. For each spectrum, the Raman features can be curve fitted, and the different line parameters (integrated intensity, line frequency, line width, background intensity) can be plotted as a function of spatial coordinates to construct images.

RESULTS AND DISCUSSION

Electrochemical behavior of new electrode

Figure 1 shows the evolution of new BDD electrode (a) on voltamperometry in HNO$_3$ 2 M+Ce(NO$_3$)$_3$ 0.1 M. For the first scanning, the first oxidation peak appears at 1.46 V, the second at 1.8 V and the O2 vapor release at 1.9 V. For the second scanning, the first peak disappears, the second with less intensity one is shifted to 1.8 V and O2 vapor release voltage is at 2.0 V. Two peaks detected are related to cerium oxidation (in HNO$_3$ medium without addition, no peaks are detected), the first one correspond to high kinetic behavior according the value of potential closely equal to thermodynamic potential (E°=1.7 V/ENH=1.45 V/ECS), the second one has a slow kinetic.
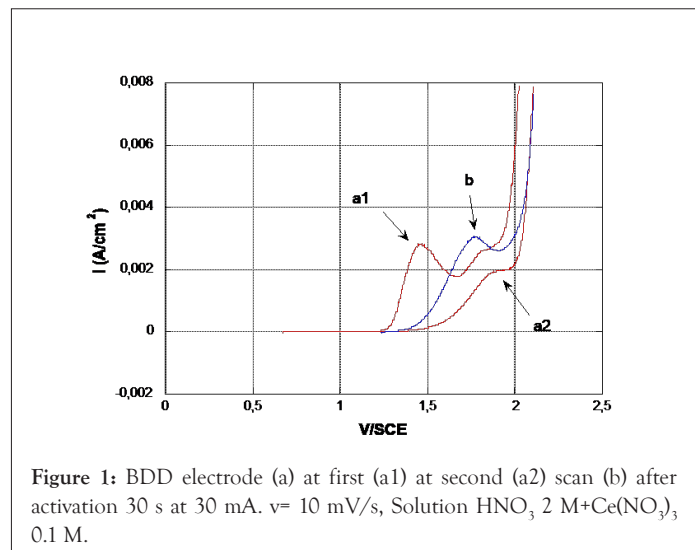

Figure 1: BDD electrode (a) at first (a1) at second (a2) scan (b) after activation 30 s at 30 mA. v= 10 mV/s, Solution HNO$_3$ 2 M+Ce(NO$_3$)$_3$ 0.1 M.

On BDD electrode (b) activated at 30 mA 60 s and at the same oxidation condition, one peak is detected with comparable intensity, at 1.77 V.

The prior oxidation of the BDD modifies the reactivity of the electrode and causes a deactivation of the fast kinetic sites with a shift of the cerium oxidation peak of 300 mV and widens the field of activity with the displacement of the oxidation potential of H$_2$O (O$_2$ evolution over potential). With a dislocation even about 300 mV. This modification, although corresponding to a decrease in the kinetics of the BDD, is often referred to as "activation". Fujishima, et al. [13], proposes either electrochemical activation of BDD by maintaining 60 min at 2.4 V/Ag/AgCl, cyclic voltamperometry between 0 and 2.5 V/ECS or by oxidation with oxygen plasma [14]. For the oxidation of phenol, Comminellis, et al. proposed to activate the electrode at E=2.84 V/ESH [15]. For the oxidation of 3-methylpyridine, authors proposed an oxidation at 60 mA/cm², approximately 3.3 V [16]. BDD oxidation modifies the reactivity of the electrode and causes the deactivation of sites responsible for rapid kinetics.

The Mott-Schottky diagrams related to BDD in the initial state are plotted by increasing potentials on the new electrode (c) in 2 M HNO$_3$. The values are given for a frequency of 1084 Hz (Figure 2). The capacitance has a straight line with a low slope up to 1.5 V corresponding to a dielectric plateau, then a straight line with a steeper slope over a narrow potential range of about 200 mV. The intersection of this line with the potential axis gives a 1.7 V flat band potential value and a doping rate of 2 10^{18} cm^{-3} carriers. As the potential increases to 1.8 V, a sharp increase of 1/C² is observed, followed by a new decreasing line that cuts the potential axis to 2 V-2.1 V.
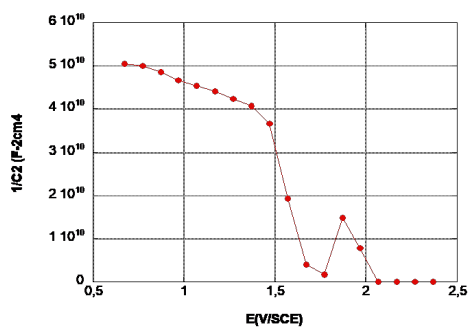
Figure 2: New-BDD electrode. Mott-Schottky Diagramme; measurements undertaken with growing potential f=1084 Hz, Solution HNO$_3$ 2 M.

This behavior of the BDD is in agreement with the model of semiconductors comprising multiple electronic states in volume [17,18] observed Mott-Schottky diagrams presenting a rupture of slope with a maximum. Mott Schottky diagrams of the BDD showed some similarity to our results have already been observed in a basic environment (slope break just before the release of oxygen) [19] but generally the Mott Schottky diagrams of the BDD are plotted in a lower potential range [9] and are extrapolated for high potential values (1.5 V to 2 V). The BDD flat-band potential values are extrapolated from the low slope that we attributed to the dielectric plateau. As a result, the BDD flat-band potential values obtained are higher (of the order of 4 V). In addition, these measurements are not performed on activated electrodes. These high values of Ebp do not explain the evolution of oxygen in the zone where the electrode has a blocking behavior. An Ebp value equal to or slightly less than the beginning of oxygen evolution is more logic and consistent with the value we obtained for the intersection of the straight line with the axis.

These results are consistent with the evolution of the properties of the BDD electrode described in the literature. According to Fujishima, et al. [13], oxidation leads to the appearance of hydroxyl functions on the surface, replacing the surface hydrogen of the mode of preparation.

In the literature, there is a large disparity in the BDD flat-band potential values. The BDD flat-plate potential treated with hydrogen plasma is 0 V/ECS in 0.1 M KH$_2$PO$_4$ and after oxidation treatment it is 1.2 V. For BDD electrodes treated with hydrogen plasma, the flat band potential is independent of pH (no hydroxylated surface functions) [20] whereas for oxidized electrodes Ebp changes with pH. In addition, there is no pH change in pH medium acid where the surface functions are not dissociated but a slope of 57 mV is observed from pH 5, which could correspond to number of dissociated surface acid sites for pH>pKa which could be of the order of 5. This behavior is similar to that of the oxides interacting with H+ and OH- [21]. Oxidation also makes it possible to eliminate sp2 residual bonds [10].

The reactivity of the BDD surface with respect to redox systems depends both on their thermodynamic potential, their pH and their charge. Indeed, the hydroxylated surface charges may exert a repellent or attractive effect. The effect is different with respect to anion (ferri-ferrocyanide, (IrCl$_6$)^3) and Fe^{II}/Fe^{III} or Ce^{III}/Ce^{IV} (positive) which are accelerated [13]. In the case of neutral molecules such as ascorbic acid, activation depends on the nature of the treatment of BDD and surface carbonyl groups. DNPH

forms covalent bonds with carbonyl groups and allows different surface properties to be demonstrated [11].

The surface bonds can be characterized by XPS: The C-C bond is characterized at 284 eV, the C-OH and C-O-C bonds at 285 eV-286 eV and carbonyl or carboxyl bonds at 287 eV [13].

Aging BDD evolution trends

After 50 h aging of the BDD, a change in the potential of the cerium oxidation peak and the release of oxygen is observed, which shows that the surface is still evolving (Figure 3) and then the peak potential remains stable up to 530 hours (Figure 4). At the return cycle, the difference between the potential of the oxidation peak and the reduction peak of the Ce^{IV} formed at the electrode increases which characterizes a decrease in kinetics. Beyond 50 h, the oxidation peak of the cerium remains stable, but the kinetics of oxygen evolution tends decrease.
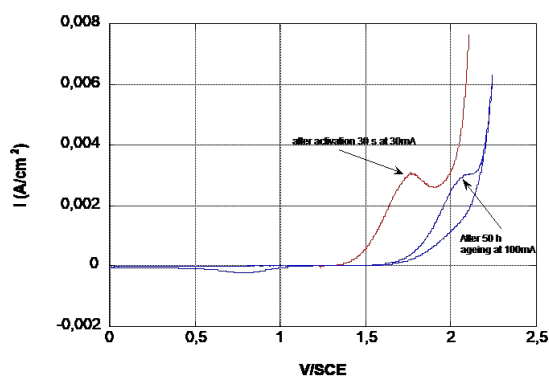

Figure 3: Evolution of oxidation peak of cerium on BDD electrode, after activation 60 s at 30 mA and after 50 h of ageing in the solution HNO$_3$ 2 M at applied current 100 mA. v= 10 mV/s, solution HNO$_3$ 2 M+Ce(NO$_3$)$_3$ 0.1 M.

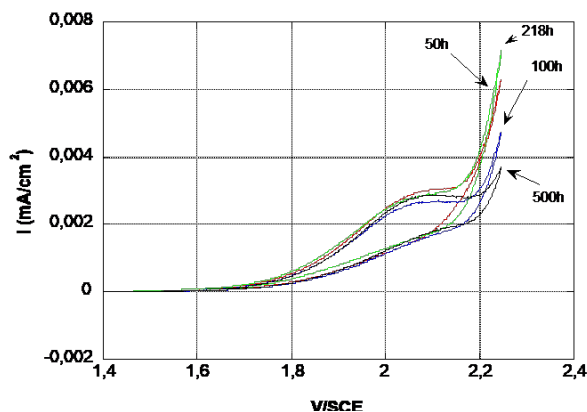**Figure 4:** Evolution of oxidation peak of cerium and oxygen evolution on BDD electrode, versus ageing time in HNO3 2 M at applied current 100 mA. v= 10 mV/s – Solution HNO$_3$ 2 M+Ce(NO$_3$)$_3$ 0.1 M.

The Mott-Schottky diagrams of BDD are plotted during aging by decreasing potential from 2.3 V (Figure 5). The value of the flat band potential is approximately 2.2 V since beyond this, the value of 1/C^2 is zero. The linear part only extends over a low potential range of 300 mV.
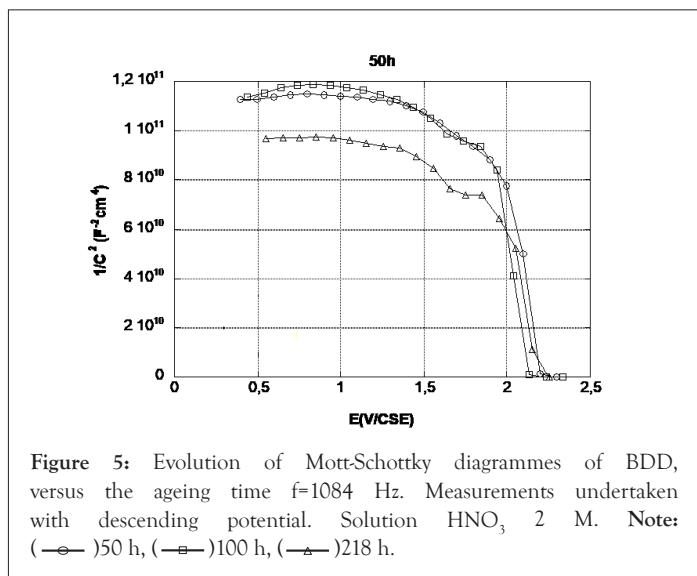
Figure 5: Evolution of Mott-Schottky diagrammes of BDD, versus the ageing time f=1084 Hz. Measurements undertaken with descending potential. Solution HNO$_3$ 2 M. **Note:** (—○—)50 h, (—□—)100 h, (—△—)218 h.

The flat band potential of the BDD has shifted to 2.2 V and this displacement is in agreement with the displacement of the oxygen evolution at this potential. However, there is still a weakly marked transition between 1.5 and 2 V corresponding to the transition observed on the new electrodes. The flat strip potential of the BDD and the slopes of the straight lines do not change during aging. The slopes are stronger than for the new electrode, and correspond to a doping rate of 3.5 10^{17} cm^{-3}, which is ten times lower than on the new electrode. This could be due to a difference in doping between two electrodes prepared in the same way or to a decrease in doping due to oxidation. Similarly the dielectric bearing is higher than that observed in the initial state.

These results confirm the existence on the BDD of an oxidized state which is accentuated during the first 50 hours of use of the electrode. After the first fifty hours, the electrode appears stable and there is no degradation of the cerium oxidation peak. There is no evolution in time between 50 and 100 h. After 218 h, the plateau observed on Mott-Schottky diagrams with low potential and related to the dielectric character of the material has a lower value (C higher, material more insulating). The flat band potential and the slope of the lines remain unchanged.

Raman results

The electrochemical data presented above reflect macroscopic film properties. Polycristalline diamond films are composed of faceted microcrystallites of different preferred orientations, grain boundaries, extended defects, and in some cases non-diamond carbon impurities. All of these factors are believed to influence the electrochemical properties in a specific way. It is well-known, for example, that the uptake of foreign atoms during diamond growth is dependent on the crystallographic orientation of the growth sector. It has been shown that boron uptake is higher on (111) facets than on (100) facets [19]. Such facets with different doping level, grain boundaries or extended defects can also present different behaviour with time working in corrosive environment. An understanding of the structure-reactivity relationship and of its evolution requires that one be able to characterize and spatially distinguish these features within the film. Raman scattering and photoluminescence spectroscopy are widely used as tools for the characterization of impurities, defects and structural imperfections in diamond films. The development of micro-Raman analysis techniques enables one to investigate the impurities, defects and

structural imperfections in diamond films with sub-micrometer resolution. Moreover, recent improvements in the implementation of the technique make Raman spectroscopic imaging possible [10,11,22-26]. Raman imaging with spatial resolution better than the size crystallites was then carried out before and after electrochemical experiments in aqueous acidic medium. Figure 6 gives a representative mean Raman spectrum recorded for a boron doped diamond sample.
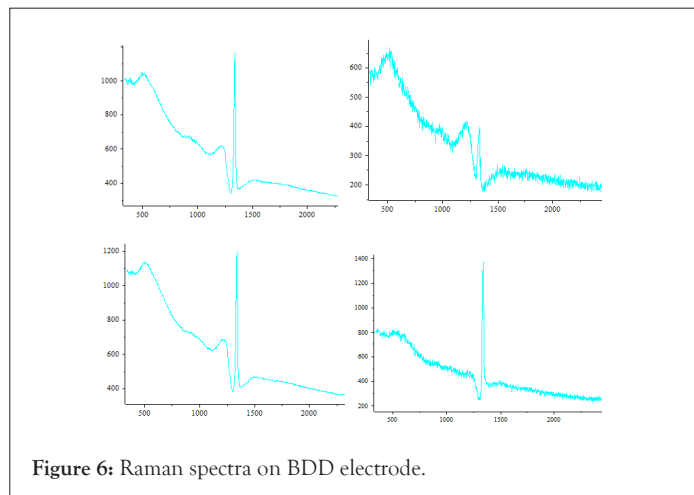

Figure 6: Raman spectra on BDD electrode.

Important Raman spectral features include (i) the frequency and intensity of the diamond line (the optical one-phonon line at approx. 1332 cm^{-1}, (ii) the diamond line width which is, to a first approximation, a measure of the crystalline quality, (iii) the frequency position of wide peaks situated at 500 cm^{-1} and 1225 cm^{-1} commonly observed for boron-doped diamond films [27,28], (iv) the scattering intensity in the region of 1400 cm^{-1}-1600 cm^{-1} due to non-diamond carbon impurities, and finally (v) the background photoluminescence intensity measured at 1650 cm^{-1} in the present work. A Fano-like line shape, characterized by an upward shift in the intensity on the high wave number side of the peak and resulting in a dissymmetrical profile is more or less evidenced on the diamond line. This Fano effect which results from the boron doping is attributed to interferences between electronic states of the boron impurity band and the optical phonon energy of diamond lattice. The doping level, in the range of 10^{19} to 10^{21} B/cm^3, can then be estimated from this dissymmetrical amplitude. An estimation of the boron doping level can also be extracted from the frequency shift of the boron wide feature peaking around 500 cm^{-1} [28].

Raman imaging results obtained on the diamond electrode before any electrochemical working are displayed on Figure 7.

Figure 7a and 7b shows the optical image of the sample, the rectangle (40 μm × 40 μm) indicates the area where the Raman data were acquired with a point spacing of 1 μm. This optical image reveals different grains, some with specific shapes, triangular for (111) facets, square for (100) facets with a mean size of 3-5 μm. Different images were constructed from the spectral data: (b) the integrated diamond line intensity, (c) the 500 cm^{-1} boron line intensity, (d) the diamond line frequency, (e) the 500 cm^{-1} line frequency, (f) the diamond line width, (g) the background photoluminescence intensity measured at 1650 cm^{-1}. The first result is that the structural features present in the optical image are less or more apparent in the constructed images. At first look, the variations in the diamond line intensity from point to point design the crystallite distribution in the film. The Raman intensity mainly depends on two factors: (i) Intensity variations from grain

to grain can reflect different instrumental response with respect to the polarization of the scattered radiation, i.e. with respect to the crystallite orientation. (ii) The darker regions can also label the less transparent regions to the focused incident laser beam, i.e. the regions were less volume sample is probed. In this case, the diamond line intensity map partially reflects the local variations in the optical absorption coefficient, and, consequently the darker regions represent the higher boron doped regions. So, it is noteworthy that these darker regions for the diamond line intensity are not exactly correlated to the regions with higher intensity for the boron related line (Figure 7c). For this sample, the 500 cm^{-1} band intensity seems not to vary as a function of the doping level. Inversely, this band intensity is largely correlated to the luminescence background as can be seen by comparing the Figures 7c-7g. It is noteworthy that the diamond line frequency (Figure 7d) and width (Figure 7f) are also little or no correlated to the boron doping level. This express that the broadening and the peak-shift of the one-phonon Raman line of diamond that can be induced by the boron doping are hidden in these films by the broadening and the peak-shift resulting from local stress fluctuations [20-22,27]. The most striking image is the one constructed with the variations of the boron feature frequency (Figure 7e), nearly super imposable to the image of the diamond line intensity variations. Several teams reported the evolution of the Raman spectra of CVD diamond with progressive incorporation of boron in the diamond lattice [19,24]. They reported that the characteristic features of the Raman spectra of B-doped diamond crystals (the two large bands at 500 cm^{-1} and 1230 cm^{-1} and the diamond line asymmetry) can be related to the boron concentration in the range of $7 \ 10^{18}$ to $2 \ 10^{21}$ B/cm^3. It was so visible that the frequency of the 500 cm^{-1} band was downshifted with the boron incorporation increase. Moreover, for equal boron concentration, (111) and (100) growth sectors exhibit a same Raman spectrum, but it was seen that (111) facets present higher boron incorporation than (100) facets at a same B/C ratio in the gas phase. So, even if the local stresses in these films are too high for the asymmetry or the broadening of the diamond line be analyzed as a function of the boron concentration, the global spectrum and the frequency of the near 500 cm^{-1} peak are reliable factors to estimate not only the mean boron concentration in the film but also the variations of the local concentration point by point as a function of the growth sectors. We can see on Figure 7f that the frequency variation of the 'boron' peak ranges from 500 to 580 cm^{-1} The Raman spectra recorded from different points permits us to estimate for the points with the higher boron concentrations a doping level of about $1 \ 10^{20}$ B/cm^3 and for the points with the lower boron concentration a doping level of about $1 \ 10^{19}$ B/cm^3. By assuming, in agreement with the measurements reported by Ushizawa, et al. [27], that the boron concentration is mainly higher in the (111) growth sectors than in the {100} ones, these values correspond to a B/C ratio in the gas phase of about 400 ppm. Figure 6 represents the mean Raman spectrum of the probed area which leads to estimate the mean boron doping level in the film less than $6 \ 10^{19}$ B/cm^3.

The same images (not presented) were obtained after the electrochemical working of the boron doped diamond electrode in a first step for 100 h, than for 500 h. Any detectable modification neither on the mean Raman spectrum nor on the individual extreme point spectra could be recorded. The two mean Raman spectra are exactly superimposable, suggesting that, in the limit of the spectrometer sensibility, the boron doping level was not affected by the electrochemical treatment
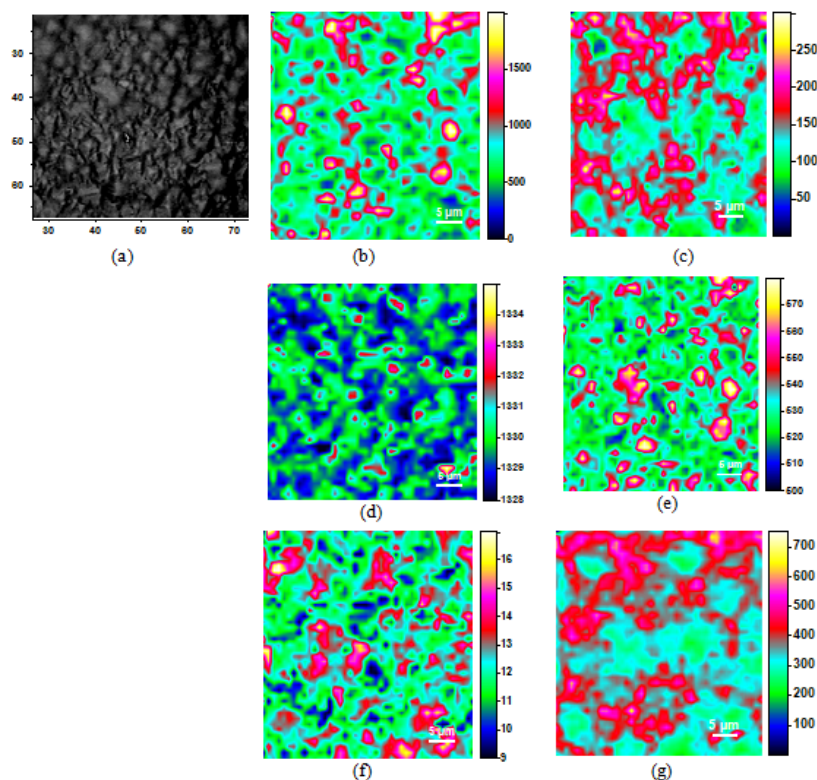

Figure 7: (a) Image optic (b) Integration of diamond line (c) Intensity of absorption line at 500 cm^{-1} of boron (d) Diamond frequency (e) Frequency at 500 cm^{-1} (f) Peak width of diamond (g) Photoluminescence at 1650 cm^{-1}.

CONCLUSION

On the BDD electrode, the oxidation leads to an enlargement of the potential window which corresponds to a decrease in the kinetics of the oxidation reduction reactions in HNO_3 2 M+Ce(NO_3)$_3$ 0.1 M medium. A transformation occurs around 1.85 V which is reflected on the Mott-Schottky diagrams by a displacement of the flat-band potential of 1.7 V to 2.1 V and in voltammetry by the positive displacement of the peak of oxidation of cerium and the release of oxygen.

The BDD flat-band potential values are measured on electrodes in the initial state in 2 M HNO_3 medium and after oxidation in the potential range used for the oxidation of cerium and not extrapolated from measurements performed at lower potential. In the initial state, the Mott-Schottky diagrams are in agreement with a model of semiconductors with multiple electronic states in volume for which one observes Mott-Schottky diagrams presenting a rupture of slope with a maximum. After oxidation, the positive displacement of the flat-band potential coincides with the displacement of the oxygen evolution and the widening of the potential window.

This process does not seem to significantly alter the level of doping that remains stable during the process. This evolution continues during the first 50 hours of aging. There is no degradation of the oxidation peak of cerium during aging.

Raman spectroscopy and SEM images also show great stability. This remarkable stability justifies the use of BDD under extreme conditions that are both very acidic and highly oxidizing.

REFERENCES

1. Panizza M, Michaud PA, Cerisola G, Comninellis C. Electrochemical treatment of wastewaters containing organic pollutants on boron-doped diamond electrodes: Prediction of specific energy consumption and required electrode area. Electrochem Commun. 2001;3(7):336-339.

2. Terashima C, Rao TN, Sarada BV, Spataru N, Fujishima A. Electrodeposition of hydrous iridium oxide on conductive diamond electrodes for catalytic sensor applications. J Electroanal Chem. 2003;544:65-74.

3. Ghazouani M, Akrout H, Bousselmi L. Efficiency of electrochemical denitrification using electrolysis cell containing BDD electrode. Desalin Water Treat. 2015;53(4):1107-1117.

4. Guenfoud F, Mokhtari M, Akrout H. Electrochemical degradation of malachite green with BDD electrodes: Effect of electrochemical parameters. Diam Relat Mater. 2014;6:8-14.

5. Abdessamad N, Akrout H, Hamdaoui G, Elghniji K, Ksibi M, Bousselmi L. Evaluation of the efficiency of monopolar and bipolar BDD electrodes for electrochemical oxidation of anthraquinone textile synthetic effluent for reuse. Chemosphere. 2013;93(7):1309-1316.

6. Abdessamad NE, Akrout H, Bousselmi L. Evaluation and optimization of textile synthetic effluent discoloration using anodic oxidation on BDD electrode: application of the experimental design methodology. Desalin Water Treat. 2013;51(16):3428-3437.

7. Ferro S, De Battisti A. Electrochemistry of the aqueous ceric/cerous redox couple at conductive diamond and gold electrodes. Phys Chem Chem Phys. 2002;4(10):1915-1920.

8. Pleskov YV, Evstefeeva YE, Krotova MD, Elkin VV, Mazin VM, Mishuk VY, et al. Synthetic semiconductor diamond electrodes: The comparative study of the electrochemical behaviour of polycrystalline and single crystal boron-doped films. J Electroanal Chem. 1998;455(1):139-146.

9. Maeda Y, Sato K, Ramaraj R, Rao TN, Tryk DA, Fujishima A. The electrochemical response of highly boron-doped conductive diamond electrodes to Ce^{3+} ions in aqueous solution. Electrochim Acta. 1999;44(20):3441-3449.

10. Lippold G, Aderhold D, Comes FJ, Grill W. Raman and photoluminescence microscopy mapping of CVD micro-diamonds. Diam Relat Mater. 1997;6(11):1587-1594.

11. Pickard CD, Davis TJ, Wang WN, Steeds JW. Mapping crystalline quality in diamond films by micro-Raman spectroscopy. Diam Relat Mater. 1998;7(2):238-242.

12. Nugent KW, Prawer S. Confocal Raman strain mapping of isolated single CVD diamond crystals. Diam Relat Mater. 1998;7(2):215-221.

13. Notsu H, Yagi I, Tatsuma T, Tryk DA, Fujishima A. Surface carbonyl groups on oxidized diamond electrodes. J Electroanal Chem. 2000;492(1):31-37.

14. Yagi I, Notsu H, Kondo T, Tryk DA, Fujishima A. Electrochemical selectivity for redox systems at oxygen-terminated diamond electrodes. J Electroanal Chem. 1999;473(1):173-178.

15. Iniesta J, Michaud PA, Panizza M, Cerisola G, Aldaz A, Comninellis C. Electrochemical oxidation of phenol at boron-doped diamond electrode. Electrochim Acta. 2001;46(23):3573-3578.

16. Iniesta J, Michaud PA, Panizza M, Comninellis C. Electrochemical oxidation of 3-methylpyridine at a boron-doped diamond electrode: Application to electroorganic synthesis and wastewater treatment. Electrochem Commun. 2001;3(7):346-351.

17. Dean MH, Stimming U. Capacity of semiconductor electrodes with multiple bulk electronic states Part I. Model and calculations for discrete states. J Electroanal Chem Interfacial Electrochem. 1987;228(1):135-151.

18. Bozzelli JW, Dean AM. Hydrocarbon radical reactions with oxygen: comparison of allyl, formyl, and vinyl to ethyl. J Phys Chem. 1993;97(17):4427-4441.

19. Van De Lagemaat J, Vanmaekelbergh D, Kelly JJ. Electrochemistry of homoepitaxial CVD diamond: Energetics and electrode kinetics in aqueous electrolytes. J Electroanal Chem. 1999;475(2):139-151.

20. Jiang Y, Liu D, Jiang Z, Mao B, Ma X, Li Q. Investigation on electrochemically cathodic polarization of boron-doped diamond electrodes and its influence on lead ions analysis. J Electrochem Soc. 2014;161(6):410-415.

21. Jolivet JP. From Solution to Oxide. Savoirs Actuels, 1994.

22. Wang J, Swain GM, Mermoux M, Lucazeau G, Zak J, Strojek JW. Probing the Microstructure and Electrochemical Reactivity of Boron-Doped Diamond Thin Film Electrodes with Raman Microprobe Spectroscopy and Electrogenerated Chemiluminescence Imaging Analysis (NDFCT 255). New Diam Front Carbon Technol. 1999;9(5):317-344.

23. Tajani A, Mermoux M, Marcus B, Bustarret E, Gheeraert E, Koizumi S. Strains and cracks in undoped and phosphorus doped (111) homoepitaxial diamond films. Phys Status Solidi. 2003;199(1):87-91.

24. Mermoux M, Marcus B, Crisci A. Confocal Raman imaging for the study of HPHT and CVD diamond crystals and films. Phys Status Solidi. 2003;199(1):97-102.

25. Mermoux M, Marcus B, Swain GM, Butler JE. A confocal Raman imaging study of an optically transparent boron-doped diamond electrode. J Phys Chem B. 2002;106(42):10816-10827.

26. Hayward IP, Baldwin KJ, Hunter DM, Batchelder DN, Pitt GD. Direct imaging and confocal mapping of diamond films using luminescence and Raman scattering. Diam Relat Mater. 1995;4(5):617-621.

27. Ushizawa K, Watanabe K, Ando T, Sakaguchi I, Nishitani-Gamo M, Sato Y, et al. Boron concentration dependence of Raman spectra on {100} and {111} facets of B-doped CVD diamond. Diam Relat Mater. 1998;7(11):1719-1722.

28. Pruvost F, Bustarret E, Deneuville A. Characteristics of homoepitaxial heavily boron-doped diamond films from their Raman spectra. Diam Relat Mater. 2000;9(3):295-299.